

Outer regions of the merging system Arp 270^{*}

A. Zasov^{1,2†}, A. Saburova¹, I. Katkov¹, O. Egorov¹, V. Afanasiev³

¹ *Sternberg Astronomical Institute, Moscow M.V. Lomonosov State University, Universitetskij pr., 13, Moscow, 119992, Russia*

² *Faculty of Physics, Moscow M.V. Lomonosov State University, Leninskie gory 1, Moscow, 119991, Russia*

³ *Special Astrophysical Observatory, Russian Academy of Sciences, Nizhniy Arkhyz, Karachai-Cherkessian Republic 357147, Russia*

June 18, 2018

ABSTRACT

Arp 270 (NGC 3395 and NGC 3396) is the system of two actively star-forming late-type galaxies in contact, which already have experienced at least one close encounter in the past. We performed long-slit observations of peripheric regions of this merging system with the 6-m telescope of SAO RAS. Line-of-sight velocity distribution along the slits was obtained for gas and stellar population. We found that the stellar component of NGC 3395 differs by its velocity from the emission gas component in the extended region in the periphery, which evidences a spatial separation of stars and gas in the tidally disturbed galaxy. Gas abundances obtained by different methods demonstrate that both galaxies are mildly underabundant ($12 + \log(O/H) \approx 8.4$) without significant variations of metallicity along the slits. By comparing stellar and gaseous masses of galaxies we came to conclusion that the chemical evolution of gas is badly described by the closed box model. It allows us to admit that the significant part of interstellar gas was swept out of galaxies during the preceding encounter(s). A special attention was paid to the extended kpc-size island of star formation between the galaxies. We have not found neither noticeable kinematic decoupling of this region from the adjacent areas, nor any peculiarities of its emission spectra, which evidences that it was formed recently from the gas of NGC 3395 in the transition region between the colliding galaxies.

Key words: galaxies: kinematics and dynamics, galaxies: individual: Arp 270, galaxies: interactions, galaxies: abundances, galaxies: ISM.

1 INTRODUCTION

Arp270 = NGC 3395/96 = VV246 = KPG 249 – is tightly interacting pair formed by two galaxies of comparable luminosities: a spiral galaxy NGC 3395 and irregular galaxy (Irr or Sm) NGC 3396, highly inclined to the line of sight. The relative motion of galaxies seems to occur in a plane perpendicular to the line of sight, because their line-of-sight central velocities nearly coincide (1625 km s^{-1} according to NED¹). The distance between the centres of galaxies is about 10 kpc. Both galaxies contain neutral and ionized gas and young stars. UV images of galaxies obtained by the Hubble telescope, revealed in both galaxies a large number of compact

and small (less than 20 pc) regions containing newly formed stars, many of which seem to form a gravitationally bound cluster (Hancock et al. 2003).

There are two features which attract a special attention to this system. First, here we have the rare case when it is safe to say that the galaxies have already experienced a strong tidal interaction at least once in the past. Indeed, H I line observations reveal the long tidal tails of gas, containing about 4×10^8 solar masses of H I, which extend over a distance of 60 kpc (see Clemens et al. 1999). H I data allowed us to obtain a large-scale picture of the distribution of radial velocities in the interacting system. Numerical modelling of interactions conducted by Clemens et al. (1999), led to conclusion that the previous convergence of galaxies took place about 5×10^8 years ago, whereas some tens of millions of years ago the galaxy once again passed the position of closest approach. The current splash of star formation is evidently associated with this latest convergence. It is worth noting that, as the simulations predict, a strong tidal stripping removes most of the original dark matter haloes of interacting

^{*} Based on observations collected with the 6 m telescope of the Special Astrophysical Observatory of the Russian Academy of Sciences, which is operated under the financial support of the Science Department of Russia (registration number 01-43).

[†] Corresponding author: zasov@sai.msu.ru

¹ <http://ned.ipac.caltech.edu/>

Table 1. Masses of H I, luminosities and the effective yields for Arp 270

Object	$\log L_K$ (L_\odot)	M_H ($10^9 M_\odot$)	$Y_{eff} \times 10^3$ M/ $L_K=1$	$Y_{eff} \times 10^3$ M/ $L_K=0.5$
NGC 3395	10.0	1.5	2.4	1.6
NGC 3396	10.1	0.92	1.6	1.2
total	10.4	2.9	1.9	1.4

galaxies (Libeskind et al. 2011), hence one can expect that the subsequent rapprochement may be more violent due to shallower potential well.

The second peculiarity of this system is the presence of numerous isolated islands of star formation, well visible in optical and especially in UV images in the outskirts of galaxies and between them. In particular, many small blue stellar regions are noticeable at the periphery of NGC 3395, in the opposite side from the companion galaxy, where, apparently, a new tidal tail begins to grow. Their detailed study is important for elucidating the mechanisms that promote a formation of stars in the regions of low average density of gas as well as the birth of dwarf tidal galaxies. The most notable detail is the extended stellar complex (named as ESC below) of about 10 arcsec \sim 1 kpc size between the galaxies, especially bright in the UV image obtained by GALEX (Smith et al. 2010) (see also Fig. 1 in this paper). If it is gravitationally bound, it can be regarded as the tidal dwarf observed in a process of formation. In any case, the fact of simultaneous birth of stars in the extended region situated in a rather rarefied medium between the interacting galaxies looks curious.

Arp 270 has a fairly complex pattern of internal motions of gas both inside and outside of galaxies. First optical kinematic measurements made by D’Odorico (1970) showed a sign of rotation of the emission gas in both galaxies. Later, the two-dimensional velocity field in the line $H\alpha$, was obtained in the framework of the project GHASP (Garrido et al. 2002; Epinat, Amram & Marcelin 2008), which confirmed the rotation of both galaxies, as well as the presence of significant non-circular velocity in the system reaching a few tens km s $^{-1}$. Zaragoza-Cardiel et al. (2013) also constructed two-dimensional map of gas velocities in this system which demonstrates the existence of radial gas motion in the central region of NGC 3396. Based on the measurements of the velocity dispersion of emission gas the authors concluded that in both galaxies star formation is associated mostly with high luminous H II regions, which apparently are connected with gravitationally bound clouds.

Masses of H I for both galaxies as well as total mass of H I (including the gaseous tail), taken from Clemens et al. (1999), are given in Table 1 parallel with the luminosity in K -band, corresponding to K_{tot} magnitudes (NED Data base) for the adopted distance 21.6 Mpc and with the effective oxygen yields which will be discussed below.

Our spectroscopic observations were aimed primarily to investigate the peripheral regions of galaxies Arp 270, their velocity distribution and the chemical abundance of gas, as well as to estimate the mean (luminosity-weighted) age of

Table 2. Observational log

Date	PA_{slit} (deg)	T_{exp} (sec)	Seeing (arcsec)
09.02.2013	93	3900	4
09.02.2013	86	3600	2.5

stellar population in order to clarify the evolutionary status of this system.

2 OBSERVATIONS AND DATA ANALYSIS

2.1 Observations and reduction

Long-slit observations of galaxy system Arp 270 were performed in 2013 February with a new universal spectrograph SCORPIO-2 (Afanasiev & Moiseev 2011) mounted at the prime focus of the 6-m Russian telescope BTA at Special Astrophysical Observatory of the Russian Academy of Sciences. Arp 270 was observed with 1 arcsec-width long slit for two different orientations that are shown in Fig. 1. Hereafter, the slit with the positional angle $PA=93^\circ$ is labelled as Slit №1 and the second slit with $PA=86^\circ$ is labelled as Slit №2. The spectra were obtained with volume-phase holographic grism VPHG1200@540 which provides spectral coverage from 3600 to 7200 Å. We used CCD chip E2V CCD42-90 2048×4600 in the 1×2 binning mode which provided a spatial scale of 0.357 arcsec pixel $^{-1}$ and spectral sampling $\approx 1.6 \text{ Å pixel}^{-1}$. Exposition time and averaged atmospheric conditions are shown in the observational log in Table 2.

The primary data reduction steps comprised of bias subtraction, flat-fielding and cosmic ray hit removal by using Laplacian filtering technique (van Dokkum 2001). We constructed the wavelength solution using the He-Ne-Ar lamp by fitting the position of lines by fifth- and fourth- order two-dimensional polynomial across and along the dispersion correspondingly, followed by linearization of spectra. The uncertainties of the wavelength solution $< 0.15 \text{ Å}$ with the mean error 0.08 Å.

To estimate a night sky spectrum, we used the peripheral regions of the slits where the contribution of galaxies is negligible. Then, the peripheral night sky spectrum was transformed into the Fourier space and extrapolated on to the galaxy position by using polynomial representation at a given frequency and after that the inverse Fourier transformation was performed. This night sky subtraction technique allows us to take into account a smoothed variation of the line spread function (LSF) of the spectrograph. Unfortunately we could not applied the previously developed advanced sky subtraction technique (Katkov & Chilingarian 2011) because it requires the reference twilight sunsky spectrum which was not obtained in the same observational nights. Final reduction steps were the summing of separately reduced object exposures and flux calibration using the spectrum of spectrophotometric stellar standard HZ4.

For the accurate extraction of stellar and emission-line kinematics (see below), we included into the model the information about LSF. Despite the absence of twilight spectrum, we mapped the LSF by fitting the Gauss-Hermite functions

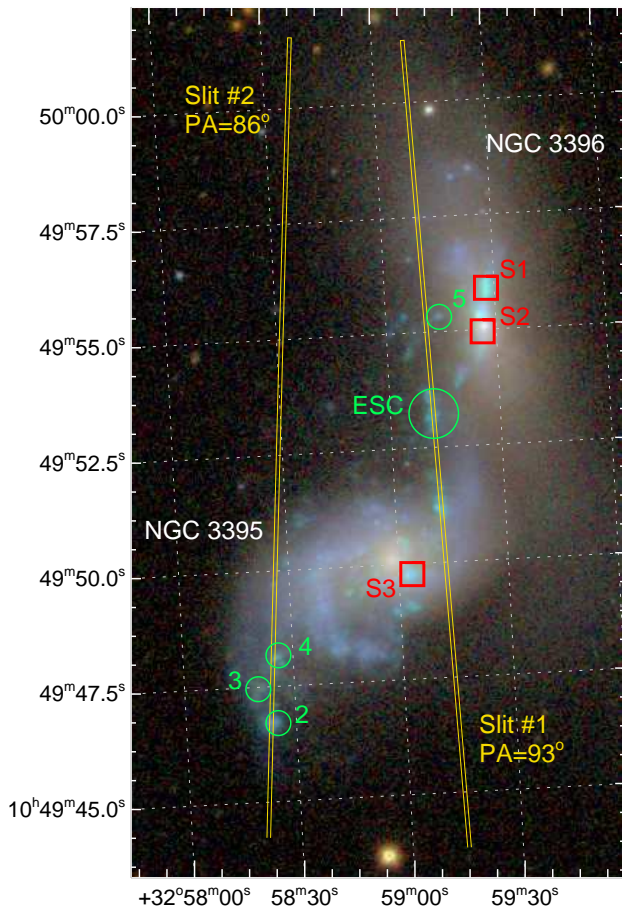


Figure 1. Composite colour map of Arp 270 based on *gri*-band images from SDSS. Long slit orientations are shown in yellow. Green circles mark star-forming regions which are discussed in the text. Red squares correspond to the positions of the SDSS aperture spectra.

up to fourth order against the lines of the arc lamp spectrum used for the wavelength calibration.

2.2 Stellar population properties

We failed to extract the continuous radial profiles of stellar population properties along the slits due to the low signal-to-noise ratio (S/N). Instead, we summarized long-slit spectra in two bins for two sections of Slit №1 and in one bin for Slit №2. The region of summation of spectra and the corresponding SNR are shown in Table 3.

Arp 270 is an actively star-forming system, therefore the contribution of young stellar population to the galaxy spectra is essential. We utilized the high-resolution ($\approx 0.3\text{\AA}$) stellar population models produced by Starburst99 syntheses code (Leitherer et al. 1999; Vázquez & Leitherer 2005). Recently, Starburst99 code was optimized for inclusion of the intermediate-age and old stellar populations by incorporation of the Padova evolutionary stellar tracks into the code that allowed us to extend the modelling to ages older than ≈ 1 Gyr and stellar masses below $0.8M_{\odot}$ (Vázquez & Leitherer 2005). We used the model templates

computed for the Padova tracks, the stellar synthetic library presented by Martins et al. (2005), the instantaneous star formation history (SSP - single stellar population) and the Kroupa initial mass function (Kroupa 2002). The final model grids are parametrized by age T and metallicity $[Z/H]$.

Stellar population parameters were derived by using a full-spectral fitting technique NBURSTS (Chilingarian et al. 2007a,b) in the special χ^2 scanning mode. This mode consists of the simultaneous non-linear, least-square fitting of parameters specified the internal kinematics in the Gauss-Hermite form (van der Marel & Franx 1993), parallel with the stellar population template pre-convolved with instrumental LSF and multiplicative continuum. The multiplicative continuum was represented by cubic spline function which connects 10 node points uniformly distributed along the wavelength. Note that the continuum fitting is of special importance because it takes into account a possible internal dust reddening as well as residual spectral slope variations due to errors in the assumed instrumental response.

In this work, we proceeded the fitting of radial velocity and multiplicative continuum only for a set of fixed values of ages, metallicities and velocity dispersions. For each combination of these model parameters ($T, [Z/H], \sigma$), we computed the optimal values of other parameters parallel with χ^2 value that finally produced χ^2 -cube in the parameter space $T - [Z/H] - \sigma$. For any acceptable values of T and $[Z/H]$ the minimal χ^2 was achieved at the lowest velocity dispersion of about 20 km s^{-1} for every bin. Taking into account the instrumental resolution ($\sigma_{inst} = 115 \text{ km s}^{-1}$), we can suggest that the stellar velocity dispersion for every bin does not exceed $0.5\sigma_{inst} \approx 60 \text{ km s}^{-1}$. The χ^2 maps for each bin are shown at Fig. 2. It shows that for each bin there exists a global minimum in the χ^2 maps. There is also a substantial age-metallicity degeneracy for Bin №2 (see zoomed subimages at Fig. 2) that appears as the noticeably stretched and inclined isolines probably caused by the low signal-to-noise ratio ($S/N = 5.5$ per pixel as about 5100\AA). The best-fitting values of stellar population parameters are presented in Table 3, the parameter errors there correspond to the range covered 1σ level at the χ^2 maps (see Fig. 2).

Note that the retrieved stellar population age T may not correspond to the epoch of formation of the entire bulk of stars because the integrated spectra for every bins keep fossil record of young, intermediate-age and old stars. The obtained SSP-equivalent stellar population parameters are rather luminosity-weighted ones for stars of all ages and metallicities. It means that the SSP-equivalent estimates are biased to properties of younger stellar populations.

2.3 Line-of-sight velocities of stars and gas

To extract the profiles of the line-of-sight stellar velocities along the slits, we divided spectra on smaller spatial bins used previously for determination of stellar population parameters by applying the adaptive binning of the long-slit spectra to achieve minimal required value $S/N=3$. Then, we fitted the binned spectra by high-resolution Starburst99 models with the fixed parameters of velocity dispersion and stellar population by varying only the line-of-sight velocity and multiplicative parameters. Stellar velocity dispersions were taken as 20 km s^{-1} , which agrees with global minima in the χ^2 -cubes. The ages and metallicities were fixed as con-

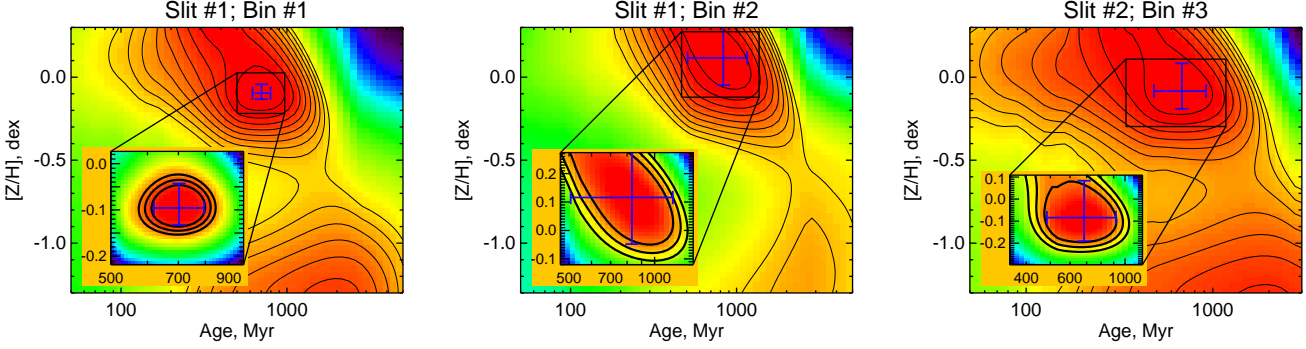


Figure 2. χ^2 -maps in the age-metallicity plane for different binned regions along slits. Black contours at the zoomed subregion of χ^2 map correspond to 1σ , 2σ , 3σ confidence levels. Blue error bars in both maps are computed by using 1σ level contour.

Table 3. Stellar population properties

Slit	Bin	Position (arcsec)	S/N	T_{SSP} (10^6 yr)	$[Z/H]_{SSP}$ (dex)
Nº 1 (PA=93°)	Nº 1	[-52,-16]	20.3	702^{+93}_{-82}	$-0.10^{+0.05}_{-0.04}$
Nº 1 (PA=93°)	Nº 2	[16, 77]	5.5	832^{+326}_{-325}	$0.12^{+0.19}_{-0.16}$
Nº 2 (PA=86°)	Nº 3	[-22, 31]	7.0	683^{+235}_{-199}	$-0.08^{+0.17}_{-0.11}$

stant values, found from the analysis of spectra in large bins, described above. The uncertainties of the velocities were estimated by Monte Carlo simulations for each spatial bin. The radial velocity profiles are shown by black symbols in Fig. 3.

The emission-line spectral component was obtained by subtracting the best-fitting stellar population model from the observed spectrum. This step provided a pure emission spectrum uncontaminated by stellar absorption lines that is important for the Balmer lines. Then we fitted emission lines with Gaussian profiles pre-convolved with instrumental LSF in order to determine the line-of-sight velocities of the ionized gas and emission-line fluxes. The velocity profiles of emission lines are shown for both slits in Fig. 3. The analysis of emission-line ratios and ionized gas abundances is presented below in Section 2.4.

2.4 Chemical abundance of ionized gas

Emission-line flux measurements allow us to get the information about the gas ionization state and its chemical composition. The distributions of emission-line fluxes and their ratios along the slits are shown in Fig. 3. The corrections for reddening were calculated from the Balmer decrement for all line fluxes. As it follows from Fig. 3, the highest values of line ratios $[O III]/[O II]$ as well as $[O III]/H\beta$ in the spectrum for PA=93° (Slit Nº1) take place in the region of star-forming ‘island’ (ESC) and slightly eastward from the compact bright star formation site at the position -25 arcsec along the slit. It gives evidence that there we have the highest ionization degree, as well as the most hard emission in comparison with the adjacent regions. In general, the ionization state smoothly decreases along Slit Nº1 from the east to the west edge.

The spectrum with PA=86° (Slit Nº2) reveals the enhanced ratio of $[O III]/H\beta$ in the most bright detached HII regions. Their ratios of $[N II]/H\alpha$ and $[S II]/H\alpha$ (0.2-0.3) are almost equal to those for the main galaxy body and correspond to the photoionization mechanism of the emission-line excitation. The enhanced line ratios $[N II]/H\alpha$ and $[S II]/H\alpha$ are mostly observed in the faintest and evidently most rarefied regions.

In Fig. 4 the diagnostic diagrams of the line fluxes ratio $[O III]/H\beta$ over $[N II]/H\alpha$ (left-hand panel) and over $[S II]/H\alpha$ (right-hand panel) are shown. The curved lines in the diagrams separate the regions of shock ionization (above) and photoionization (below; see Kewley et al. 2006). In the left-hand panel of Fig. 4 several ‘composite’ regions with the mixed excitation mechanism are located between the grey and black lines.

In the diagnostic diagrams we marked the regions with different intensity levels by different symbols: bright regions ($F(H\alpha) > 10^{-15} \text{ erg s}^{-1} \text{ cm}^{-2}$) we denoted with filled circles, while faint regions ($F(H\alpha) < 10^{-15} \text{ erg s}^{-1} \text{ cm}^{-2}$) are marked by the open circles. Crosses in the diagnostic diagrams mark the positions of the ESC region. One can see that for all studied bright regions (including ESC) a photoionization is the dominant mechanism of excitation, while the presence of the shock waves appears in some faint diffuse regions only.

For the detailed investigation of gas chemical abundance (metallicity), we have to know the electron temperature of the emission regions. Electron temperatures T_e of high and low excitation regions may be found from the measurements of emission lines $[O III] 4363\text{\AA}$ and $[N II] 5755\text{\AA}$ fluxes sensitive to T_e (see e.g. Pilyugin et al. 2009). However, these lines are faint, and we were able to get the accurate measurements of these lines only for several regions. The location of these regions along the slit and the corresponding

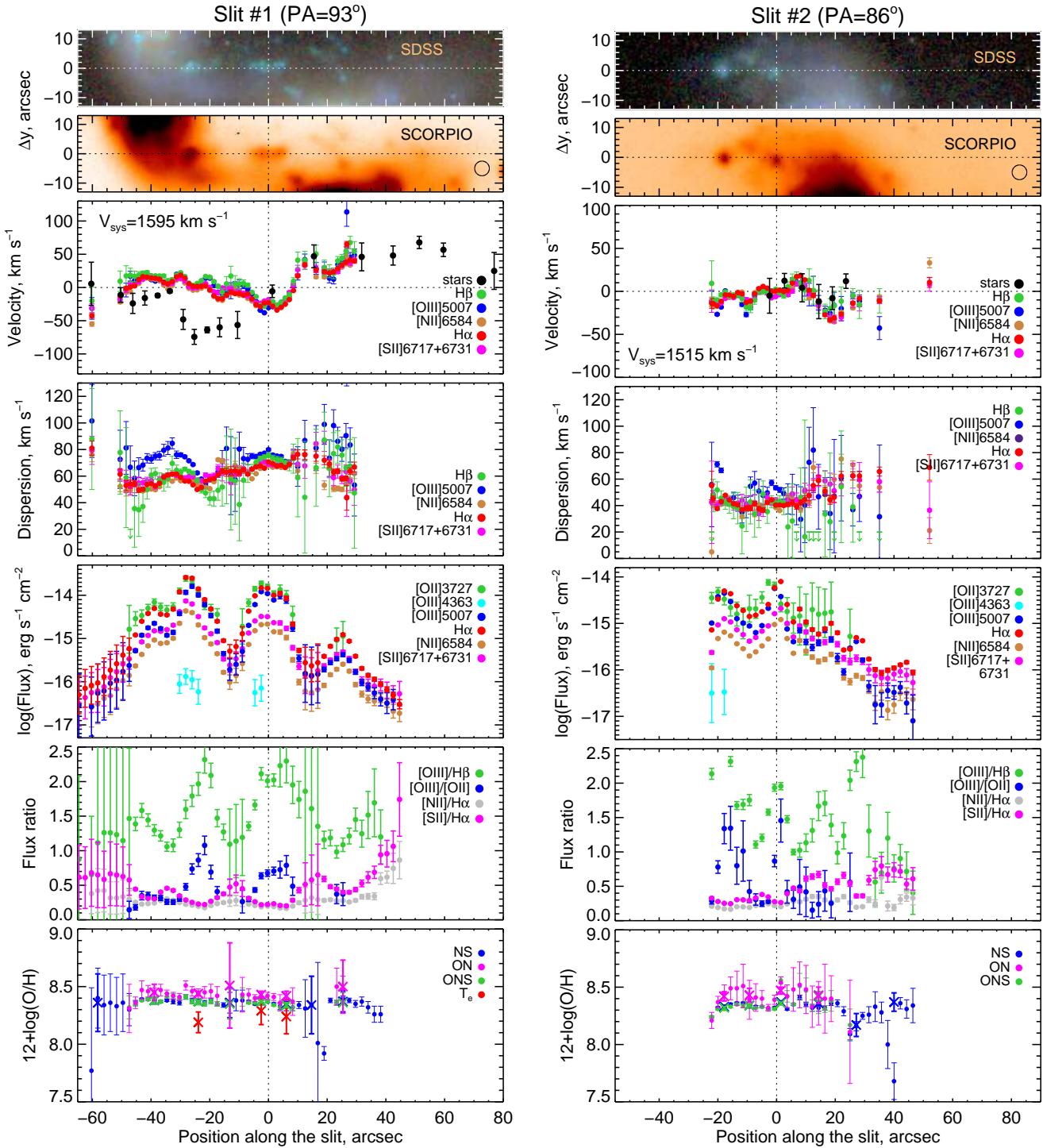


Figure 3. Radial profiles of the line-of-sight velocity and velocity dispersion and distribution of emission-line fluxes, flux ratios and oxygen abundances measured for both slits; (*left* Slit №1 (PA=93°), *right* - Slit №2 (PA=86°)). Two top panels present the reference images taken from SDSS and obtained at SCOPRIO in the image mode. Black circle describes the atmospheric seeing. Next two panels reproduce the line-of sight velocities and velocity dispersions. Zero level of velocities (V_{sys}) are given in the panels. Black symbols correspond to stellar kinematics, colour circles to different emission lines. The zero- points on the x -axes correspond to the most bright regions at the slits. Bottom three panels present the fluxes of measured emission lines, line flux ratios and oxygen abundances calculated by different methods (see details in Section 2.4). Crosses in the bottom panels indicate the results obtained using the fluxes integrated over the regions with larger binning.

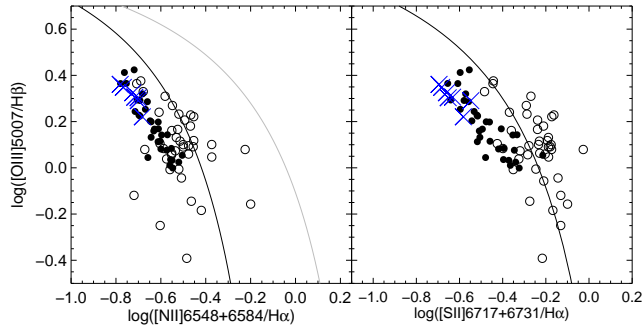


Figure 4. Diagnostic diagrams for studied bins along both slits. Open circles denote faint bins with $F(\text{H}\alpha) < 10^{-15} \text{ ergs}^{-1} \text{ cm}^{-2}$, while filled circles correspond to bright regions $F(\text{H}\alpha) > 10^{-15} \text{ ergs}^{-1} \text{ cm}^{-2}$. Position of ESC is marked by blue crosses. Black curved line separates the pure photoionization regions from the regions with the shock excitation (following Kewley et al. 2006). Regions with the mixed ionization mechanism lay between the black and grey lines in the left diagram.

oxygen abundance are shown in Fig. 3 and denoted with red crosses.

Applying the equations from Izotov et al. (2006), we estimated the abundances of oxygen, nitrogen, sulphur, argon, neon, iron and chlorine using the direct T_e -method for regions with available T_e estimations. The median obtained values are: $12 + \log(\text{O}/\text{H}) = 8.22 \pm 0.13$, $\log(\text{N}/\text{O}) = -1.10 \pm 0.14$, $\log(\text{S}/\text{O}) = -1.77 \pm 0.16$, $\log(\text{Ne}/\text{O}) = -0.78 \pm 0.26$, $\log(\text{Ar}/\text{O}) = -2.53 \pm 0.15$, $\log(\text{Fe}/\text{O}) = -2.01 \pm 0.14$, $\log(\text{Cl}/\text{O}) = -3.55 \pm 0.15$. These calculated chemical abundances relative to oxygen abundance are in good agreement with the mean values for other spiral galaxies (Izotov et al. 2006).

As far as the photoionization excitation mechanism dominates in the investigated regions, we may conclude that most probably emission lines are produced by non-resolved HII regions. In this case we are able to use the empirical methods for metallicity estimations calibrated by the data for HII regions with available accurate measurements of T_e . We applied three of these methods to our data:

- ONS-method (Pilyugin, Vilchez & Thuan 2010), that uses the flux ratios of $[\text{O II}]3727+3729$, $[\text{O III}]4959+5007$, $[\text{N II}]6548+6584$, $[\text{S II}]6717+6731$ lines to $\text{H}\beta$
- ON-method (Pilyugin et al. 2010), that uses the ratios of $[\text{O II}]3727+3729$, $[\text{O III}]4959+5007$ line fluxes to $\text{H}\beta$
- NS-method (Pilyugin & Mattsson 2011), that does not demand the knowledge of intensity of emission line $[\text{O II}]3727+3729$. Instead, it uses the line flux ratios of $[\text{O III}]4959+5007$, $[\text{N II}]6548+6584$, $[\text{S II}]6717+6731$ to $\text{H}\beta$.

The distribution of oxygen abundance along the slits, found by different methods is shown in Fig. 3 (bottom panels). ON, NS and ONS methods give similar results. The mean metallicity $12 + \log(\text{O}/\text{H}) = 8.35 \pm 0.11$ is slightly higher than that obtained by ‘direct’ T_e -method for regions with available T_e estimations.

In addition, we found three spectra for studied galaxies in the SDSS archive which positions are shown in Fig. 1. Unfortunately, their spectral range does not cover the $[\text{O II}]3727$ line that is necessary for oxygen abundance estimation by

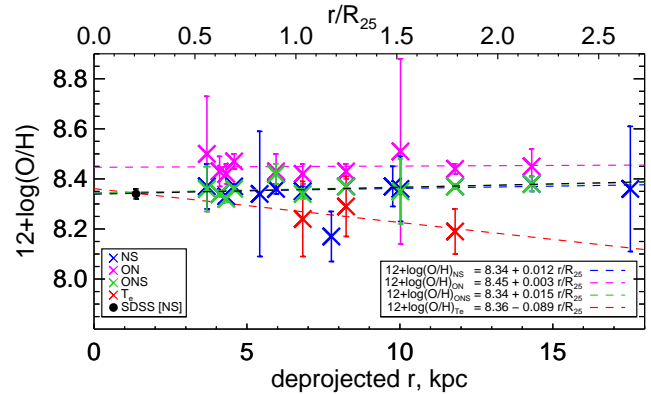


Figure 5. Radial distribution of oxygen abundance in the NGC 3395 galaxy obtained by different methods (see text). Crosses denote the same as in Fig. 3, black point denotes the result obtained with SDSS data. The linear robust fits of oxygen abundance distribution for different methods are shown with dashed lines of corresponding colour.

T_e -method. We were able to measure the metallicity from these spectra only using the NS method. The values of $12 + \log(\text{O}/\text{H})$ obtained were 8.37, 8.44 and 8.34 corresponding to S1, S2, S3 marks in Fig. 1, that are very close to the measurements described above for our spectra.

The main feature of the obtained oxygen abundance distribution is the absence of metallicity gradient. To demonstrate it, we give the plot of radial distribution of metallicity in Fig 5. In this figure the mean values of gas metallicity $12 + \log(\text{O}/\text{H})$ are plotted against their deprojected distance from the centre of NGC 3395 galaxy (in terms of kpc and of $R_{25} = 6.6$ kpc fraction). We made the deprojection assuming inclination angle $i = 57.8^\circ$ and major axis position angle $\text{PA} = 35^\circ$ (from HyperLeda² data base; Makarov et al. 2014). As it follows from Fig. 5, the gas metallicity is almost the same for all investigated regions being close to those found from the SDSS data for the inner galaxy. The metallicity gradients obtained for each methods are very low or negligible. Largest gradient ($-0.089 \pm 0.091 \text{ dex}/R_{25}$) is given by T_e method using only three available data points with large uncertainties. But even in this case, the gradient is low in comparison with normal galaxies. Of course, our observational data do not provide a dense sample of oxygen abundance measurements at different galactocentric distance and 3D spectroscopy observations of this system are needed to strength this conclusion. Nevertheless, if the metallicity gradient was high, we would have found it.

3 DISCUSSION

3.1 Stellar and gaseous kinematics

The distribution of line-of-sight velocity along the Slit №1 (Fig. 3, left-hand panel) which runs approximately parallel to the line connecting the centres of galaxies, confirms the opposite directions of radial velocity gradients of two galaxies found in the earlier papers (see the Introduction).

² <http://leda.univ-lyon1.fr/>

There is a good concordance between the velocity measurements for different emission lines. Significant irregularities of velocity distributions reveal the existence of non-circular motions of gas in a kpc-scale; however, they are not as large as those found in the inner parts of galaxies. Most notable changes of the velocity coincide with the bright emission areas, although the most extended emission region in the Slit №1 (ESC) does not manifest itself on the velocity profile. There is a steep velocity gradient in the region between galaxies (Slit №1) accompanied by grow of velocity dispersion – evidently as the result of direct contact of gaseous systems of two galaxies. Note that the brightest emission region (ESC) lies at the beginning of this transition region between galaxies. Similarly, steep gradient is also presented in the second cut (Slit №2) where the slit crosses the outer regions of NGC 3395 near its major axis. It evidences strong ($\approx 50 \text{ km s}^{-1}$) perturbations of the velocity field in the region where the short tidal tail seems to grow.

Stellar line-of-sight velocities agree with the gaseous ones with the exception of the extended region of about 3 kpc length between the main body of NGC 3395 and the emission region ESC (Fig. 3). There the stellar velocities are up to 50 km s^{-1} lower than the emission gas velocities observed along the same lines of sight. There is no such discrepancy along the Slit №2. Although the surface brightness of this region is rather low, small error bars demonstrate a reliability of estimates. The low-velocity stellar component hardly may be ascribed to the second galaxy, because its adjacent side is the receding one, having a larger line-of-sight velocity. Gas velocity field of both galaxies reveals a strong non-circular motion, although a rotational pattern of the velocity field of NGC 3395 is evident (Zaragoza-Cardiel et al. 2013). Measured velocities of emission gas (Zaragoza-Cardiel et al. 2013) and H I (Clemens et al. 1999) in this area are several tens km s^{-1} above the velocity of galaxy centre due to the disc rotation, whereas our measurements give the velocities of stars which are several tens km s^{-1} lower than that of gas. The most natural explanation of the discrepancy is that the gas and stars are spatially separated there because of strong disc tidal distortion, so that the stellar disc is more face-on oriented than the gas layer in the region crossed by the slit, and, as a result, its rotational velocity component is small. Certainly, to get a detailed picture of stellar kinematics, we need a two-dimensional stellar velocity field, which is absent now.

We compared the velocity range estimated in this paper with that of the velocity field of Zaragoza-Cardiel et al. (2013). For the Slit №1, we got the velocity variance of $\Delta v \approx 1565 - 1655 \text{ km s}^{-1}$ for ionized gas ($1535 - 1655 \text{ km s}^{-1}$ for stars). The velocity range given by Zaragoza-Cardiel et al. (2013) in the slit region is $\Delta v \approx 1590 - 1650 \text{ km s}^{-1}$. This dispersion is lower than it follows from our observation; however, the mean velocities of ionized gas agree satisfactorily. For Slit №2 the situation is similar. The estimated velocity range is $\Delta v \approx 1485 - 1535 \text{ km s}^{-1}$ in this paper. The velocity field of Zaragoza-Cardiel et al. (2013) gives $\Delta v \approx 1490 - 1550 \text{ km s}^{-1}$ for this region. Note however that the velocities found from H I observations with low spatial resolution (Clemens et al. 1999) are systematically higher than our estimations at about 60 km s^{-1} , although the signs of velocity gradients for both slits are the same.

Fig. 3 also presents the velocity dispersion of gas calculated from the instrumental profile-corrected line widths. Our measurements confirm a high velocity dispersion of ionized gas obtained from different emission lines ($\approx 50 - 70 \text{ km s}^{-1}$), previously found by Zaragoza-Cardiel et al. (2013) for the main bodies of both galaxies. Note that the velocity dispersion in excess of 40 km s^{-1} almost never occurs in normal mildly star-forming galaxies, instead it is usually observed only in galaxies with the highest luminosity in the H α line. In galaxies with moderate star formation rate, the observed dispersion usually lays in the range of $20 - 40 \text{ km s}^{-1}$ (see e.g. Moiseev, Tikhonov & Klypin 2014). In the case of Arp 270, the highest values of velocity dispersion (up to 80 km s^{-1}) accompanied by the high excitation line O[III]5007 are observed in the regions most close to the centres of galaxies, which evidently reveals the presence of shock waves there.

It is worth mentioning that both slits avoid the central parts of galaxies, where star formation is most active. A cause of high velocity dispersion of gas may be either internal velocity dispersion inside of large H II regions, or the spread of relative velocities of separate star-forming regions on the scale of linear spectral resolution (hundreds of parsecs), or both. The fact that the velocity dispersion remains high between the observed H II-regions gives evidence against the first version. Most probably, it reflects a small-scale turbulence due to gas perturbations fed by tidal forces. It is worth noting that the velocity dispersion of the cold gas (H I) obtained by Clemens et al. (1999) for the angular resolution of $\sim 21 \text{ arcsec}$ is about 27 km s^{-1} (for NGC 3395), which is also higher than the typical values $10\text{--}15 \text{ km s}^{-1}$ for star-forming galaxies. A large velocity variance along the slit in the eastern part of NGC 3396, where, apparently, a tidal tail forms, evidences that the gas velocity field is very complex there due to tidal streams of gas.

As for the stellar velocity dispersion, we failed to measure it reliably even using the binning to combine the adjusted regions. We may conclude however that it is highly probable that it does not exceed 50 km s^{-1} .

3.2 Oxygen abundance and yield

The most important feature of the abundance distributions along the slits is the absence of significant gradients of metallicity, although the better spatial coverage of the spectroscopy is needed to make firmer conclusion. Note that the low radial gradient of metallicity is quite common situation for the outer H II-regions and for interacting systems (Werk et al. 2010, 2011; Sánchez et al. 2014; Miralles-Caballero et al. 2014). Among the proposed mechanisms of smoothing, the abundance gradient well appropriate for our case, is the radial mixing of metals caused by tidal torques (Rupke, Kewley, & Barnes 2010). The most puzzling circumstance in the case of Arp 270 is that, unlike spiral galaxies, where the abundance gradient usually flattens in the outer disc, in our case the abundance remains approximately the same all around the system inspite of the significant range of radial distances covered by the slits (see Fig. 5). Different methods of the abundance estimates give the oxygen abundance $12 + \log(O/H) \approx 8.4$. Spectral data presented by Sloan Survey after the data processing, similar to that we used above, give nearly the same abundance

$12 + \log(O/H) \approx 8.4$ for the central parts of both galaxies (see Section 2.4) as we observe in the outskirts of the system.

It is essential that we estimated the metal abundance of gas continuously along the slit, not for selected high luminous HII regions. Hence, the metallicity we found is not a result of self-enrichment of massive star-forming clouds, which shows that the elements are more or less homogeneously distributed in the interstellar medium. It is evident that there is no enough time for gas mixing since the previous encounter of galaxies if to assume that the metal mixing spreads out with the turbulent velocity of gas. To get the effective missing, we need either the extended gas flows or the mixing via a hot gas phase (see the discussion by Werk et al. 2011).

Taking solar oxygen abundance as $12 + \log(O/H) = 8.7$ (Asplund et al. 2009), we find that the oxygen abundance in Arp 270 is about 1/2 solar value, which is close to the metallicity of gas in spiral galaxy M33. According to Magrini et al. (2010), the mean abundance O/H in M33 varies between 8.4 (inner part of the disc) and 8.2, that is the gas metallicity 1/2 – 1/3 of solar value. Indeed, the size and luminosity of both galaxies in Arp 270 are not very different from those for M33. The difference, however, is noticeable when comparing the relative mass of the gas with respect to the stellar mass of galaxies. Total mass of H I in M33 is $3.2 \times 10^9 M_\odot$ (Corbelli 2003), which is about a half of total mass of the disc according to the mass model of this galaxy (Saburova & Zasov 2012), that is the gas and stellar components of the disc are comparable by mass. On the other hand, for Arp 270 this ratio is much lower. Let us assume that M/L_K of stellar population lays between 0.5 and 1.0 solar units, as stellar population models predict for star-forming galaxies (see e.g. (Bell & de Jong 2001; Bell et al. 2003)). Then from the data presented in Table 1, it follows that the gas-to-star mass ratios M_{gas}/M_* for the system as whole is 25-12.5% (the latter value is for $M/L_K=1$). Here, the presence of helium is taken into account. We neglect molecular gas in galaxies: its mass is usually much less than the mass of H I. Indeed, direct measurements of CO emission for the larger of the galaxies - NGC 3395 - gave mass ratio H I/H₂ ~ 21 (see tables 11, 12 in Boselli, Cortese & Boquien 2014). If the enriched gas is well mixed, and the enrichment due to stellar evolution may be considered as instantaneous, then the simple closed box model is acceptable. In this model, the oxygen abundance is connected with the relative mass of gas $\mu = M_{gas}/(M_{gas} + M_*)$ and with the yield Y_o of oxygen per the mass of a single generation of stars by the simple relation:

$$Y_o = \frac{12(O/H)}{\ln(1/\mu)}.$$

It is convenient to introduce the effective yield, Y_{eff} , as the yield determined from the equation above for the closed box model, which in general may be too simple to be correct. Accretion, as well as the outflow of gas reduces the effective yield, so that $Y_{eff} < Y_o$ (Edmunds 1990; Spitoni et al. 2010). Hence, a comparison of the observed estimates of Y_{eff} with the expected oxygen yield Y_o allows us to reveal the peculiarities of chemical evolution of interstellar gas in a given galaxy. Theoretically obtained values Y_o are very uncertain because they depend on many factors which

are difficult to take into account (see e.g. a discussion in Pilyugin, Thuan & Vílchez 2007). More reliable estimates are based on the statistically determined upper boundary of Y_{eff} which is assumed to be close to Y_o (Pilyugin et al. 2007). Using this approach, Pilyugin et al. (2007) found the most probable value $Y_o = 0.035$, which agrees with Dalcanton (2007) results $Y_o = (4 \pm 1) \times 10^{-3}$ for galaxies having the velocity of rotation $V_c > 100 \text{ km s}^{-1}$. The measured values of Y_{eff} for M33 (Saburova & Zasov 2012) and M51 (Bresolin, Garnett & Kennicutt 2004) agree with these estimates for a wide range of radial distances.

Table 1 gives the Y_{eff} estimates obtained for the oxygen abundance $12 + \log(O/H) = 8.4$ for both galaxies in Arp 270 separately, and for this system as a whole. The latter estimate should be the most representative one because of the evident gas exchange between two galaxies. The data clearly demonstrate that Y_{eff} for this system is lower than expected for closed box model. If to apply this model using $Y_o = 0.0035$, then the ratio M_{gas}/M_* for Arp 270 should be about 42%, which is much higher than the observed ratio (see Table 1). Note that the T_e method gives (although uncertain) even lower (O/H) ratio, which, if to accept it, will make a discrepancy with the closed box model even deeper.

Most likely, the low Y_{eff} for Arp 270 is the result of significant gas losses experienced by the system during the previous convergence(s) of galaxies. The lost gas should be hot and ionized, otherwise it would be visible in H I-line as neutral intergalactic gas. Indeed, a neutral gas is observed in the remnant of tidal tails in Arp 270, but it contains only a small fraction of the present-day H I in galaxies. Is the bulk of lost gas ionized?

Note that the ionized gas mixing as the mechanism of levelling off the abundance gradient agrees with the expected short time of gas exchange between galaxies, although the details of this process remain not clear. Diffuse X-ray gas is really presented in Arp 270, as the *Chandra* observatory shows; however, it is observed within the optical borders of galaxies only (Brassington, Read & Ponman 2005): the gas outflow may be developed at later stage of interaction (Brassington, Ponman & Read 2007). Another way to account for the low gradients of metallicity is to assume that the accretion of enriched extragalactic gas on to the discs of galaxies took place after their formation. To explain the observed O/H ratio, the accreted gas should possess about 1/2 - 1/3 of solar metallicity, which is typical for gas in clusters of galaxies independently on their total stellar masses (Renzini & Andreon 2014). Although Arp 270 is quite isolated interacting system, it is located at the periphery of NGC 3430 group, being its possible member (the distance between Arp 270 and NGC 3430 is about 29 arcmin or 180 kpc). However, there is no evidence of the intracluster gas in this group, which makes the latter version doubtful.

3.3 Ages of blue stellar islands

Both slits passed through several blue islands of star formation, easily visible in the images of Arp 270 both on the emission and in the continuum. The brightest emission region crossed by Slit №1 is ESC (see above). It is the site of the active star formation, containing several (at least two) stellar agglomerates within the kpc-size region. The emission spectrum of ESC does not differ significantly from the

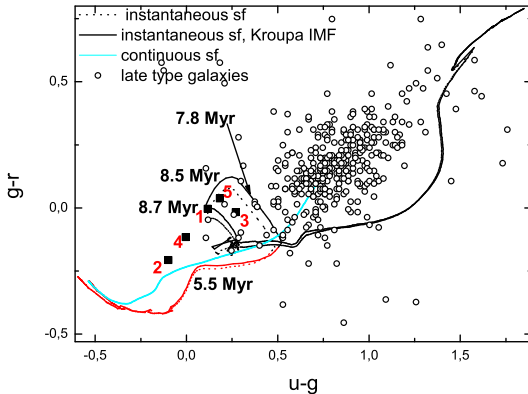


Figure 6. The $(g-r) - (u-r)$ diagram. Squares denote the positions of bright emission regions of Arp 270 (1 corresponds to ESC). Black lines correspond to Starburst99 model tracks obtained for IMF described by two exponents (see text). Blue line corresponds to the Starburst99 model for continuous star formation. Open circles mark the positions of integrated colours of bright ($B < 13^m$) irregular galaxies (morphological type $T_{morph} > 7$ according to HyperLeda data base). Red line marks the region of the diagram where the influence of emission lines on the colour indices may be significant.

spectra of other HII regions by the line intensity ratios. It also does not stand out by its abundance or by kinematics, being close to the adjacent regions of NGC 3395 by its line-of-sight velocity. Hence, the stellar island was formed from the gas belonging to this galaxy, rather than appeared as a result of accretion or minor merging.

Fig. 6 presents the positions of several bright emission regions of Arp 270 including ESC (1) on the two-colour diagram $(g-r) - (u-r)$ (see Fig. 1 for their location). The data for these regions were obtained from the photometry based on the SDSS sky survey images after correction for extinction. For comparison, the positions of integrated colours of bright ($B < 13^m$) irregular galaxies (morphological type $T_{morph} > 7$) are given, obtained from the observed UBV colours taken from the HyperLeda data base. A high dispersion of the total colour indices is mainly due to irregular character of star formation in the late-type galaxies and due to the estimate errors. The colour indices of chosen HII regions galaxies are bluer than those for the Irr galaxies because the latter contain a mixture of old and young stellar populations, whereas old stars are absent if we observe the beginning of star formation. To estimate the ages of stars, we used Starburst99 evolution tracks for different histories of star formation: instantaneous star formation with the IMFs described by two exponents of 1.3 and 2.3 (solid black line) and 1.3 and 2.0 (dash black line) for low (from 0.1 to 0.5 M_{\odot}) and high (from 0.5 to 100 M_{\odot}) masses, respectively, and for continuous star formation (blue line). Each point of the tracks corresponds to the different age of stellar population. For instantaneous and continuous star formation, we considered the following ranges of age of stellar population respectively: 1×10^{-2} Myr - 10 Gyr, 1×10^{-11} Myr - 10 Gyr. We also mark in the Fig. 6 the age of stellar population which corresponds to the closest point of the track to

the considered regions of star formation. Red line shows the region of extremely young population ($T < 6$ Myr) where the influence of emission lines on the colour indices which here we ignore may be significant (Smith et al. 2008). As the diagram shows, star formation in all considered regions has begun recently. The regions 2 and 4 are especially young, and their positions fit the evolution tracks not so good (colour indices of young population strongly depend on the heavy part of IMF and on the presence of emission lines). In turn, the regions ESC (1), 5 and 3 consist of stars formed 8 – 9 Myr ago without the evidences of the presence of old stars.

Applying this result to ESC, we may conclude, that star formation in this extended stellar island began recently. There may be two scenarios of formation of this stellar island. First, the massive gaseous complex might already exist in NGC 3395 before the convergence of galaxies, so that the tidal force swept it out together with more rarefied gas. In this case, ESC may be considered as gravitationally bound and long-living gaseous agglomerate with the star formation delayed until recent epoch, so it has a chance to become a tidal dwarf galaxy. This way of evolution of massive gas clouds was discussed in Zasov & Kasparova (2014). However, the line-of-sight velocity distribution along ESC does not give any evidence of its kinematic decoupling which casts doubt on this interpretation. Secondly, ESC may be formed as the result of the compression of gas in the colliding large-scale gaseous flows induced by close interaction between galaxies. It agrees with the position of ESC in the transition region where the line-of-sight velocities of gas begin steeply change from the values which may be ascribed to NGC 3395 to those corresponding to NGC 3396.

4 GENERAL CONCLUSIONS

- We obtain the line-of-sight velocities of gas and stars and chemical abundances distributions along the two slits crossing the peripheral regions of the interacting galaxies. Irregular velocity distribution and the high velocity dispersion of emitting gas which stems from the profiles of emission lines evidences the non-circular gas flows at small scales up to ≈ 1 kpc. We found that the stellar component of NGC 3395 differs by its velocity from the emission gas component at about 50 km s $^{-1}$ in the extended region cut by the slit in the periphery of NGC 3395, which evidences a spatial separation of stars and gas in the tidally disturbed galaxy.
- The ratio of emission lines along the slits evidences that they are produced by non-resolved HII regions. Their velocity dispersion is high (~ 50 km s $^{-1}$) in comparison with normal star-forming galaxies.
- The abundance estimates of oxygen obtained by different methods reveal the absence of significant gradients of metallicity. The oxygen abundance is found as $12 + \log(O/H) \approx 8.4$, that is the gas metallicity of about a half of solar value. Either there was an effective mixing of gas inside of galaxies and between them, or (less probable), we observe the result of accretion of initially enriched gas on to the galaxies.
- Assuming a constant (O/H) along the system, we demonstrate that the system is badly described by the closed box model: the effective yield of oxygen Y_{eff} is significantly

lower than expected one for closed box model, although 3D spectroscopy is needed to strengthen this conclusion. Low Y_{eff} may be explained by gas losses experienced by the system during the previous convergence(s) of galaxies.

- Colour indices (ugr) of several discrete sites of star formation beyond the inner regions of galaxies were estimated from the SDSS data. They confirmed the young age ($T < 10^7$ yr) of stellar population. The extended kpc size island of star formation (ESC) observed between the galaxies does not stand out by its kinematics or abundances, so it hardly may be considered as the tidal dwarf candidate. Its location at the beginning of transition zone between galaxies allows us to propose that its formation is the result of compression of colliding gas flows of galaxies in contact.

ACKNOWLEDGEMENTS

The observations at the 6-meter BTA telescope were carried out with the financial support of the Ministry of Education and Science of the Russian Federation (agreement No. 14.619.21.0004, project ID RFMEFI61914X0004). We are grateful to the anonymous referee for the valuable comments and advices. In this study, we used the SDSS DR9 data. Funding for the SDSS and SDSS-II has been provided by the Alfred P. Sloan Foundation, the Participating Institutions, the National Science Foundation, the U.S. Department of Energy, the National Aeronautics and Space Administration, the Japanese Monbukagakusho, the Max Planck Society, and the Higher Education Funding Council for England. The SDSS website is <http://www.sdss.org/>. This research has made use of the NASA/IPAC Extragalactic Data base (NED) which is operated by the Jet Propulsion Laboratory, California Institute of Technology, under contract with the National Aeronautics and Space Administration. We acknowledge the use of the HyperLeda data base. This work was supported by Russian Foundation for Basic Research (projects Nos. 12-02-00685 and 14-22-03006-ofi-m). IYK is also grateful to Dmitry Zimin's non-profit Dynasty Foundation.

References

- Afanasiev V. L., Moiseev A. V., 2011, *Baltic Astronomy*, 20, 363
- Asplund M., Grevesse N., Sauval A. J., Scott P., 2009, *ARA&A*, 47, 481
- Bell E. F., de Jong R. S., 2001, *ApJ*, 550, 212
- Bell E. F., McIntosh D. H., Katz N., Weinberg M. D., 2003, *ApJS*, 149, 289
- Boselli A., Cortese L., Boquien M., 2014, *A&A*, 564, A65
- Brassington N. J., Ponman T. J., Read A. M., 2007, *MNRAS*, 377, 1439
- Brassington N. J., Read A. M., Ponman T. J., 2005, *MNRAS*, 360, 801
- Bresolin F., Garnett D. R., Kennicutt, Jr. R. C., 2004, *ApJ*, 615, 228
- Chilingarian I., Prugniel P., Sil'Chenko O., Koleva M., 2007a, in *IAU Symposium*, Vol. 241, IAU Symposium, Vazdekis A., Peletier R., eds., pp. 175–176
- Chilingarian I. V., Prugniel P., Sil'Chenko O. K., Afanasiev V. L., 2007b, *MNRAS*, 376, 1033
- Clemens M. S., Baxter K. M., Alexander P., Green D. A., 1999, *MNRAS*, 308, 364
- Corbelli E., 2003, *MNRAS*, 342, 199
- Dalcanton J. J., 2007, *ApJ*, 658, 941
- D'Odorico S., 1970, *ApJ*, 160, 3
- Edmunds M. G., 1990, *MNRAS*, 246, 678
- Epinat B., Amram P., Marcelin M., 2008, *MNRAS*, 390, 466
- Garrido O., Marcelin M., Amram P., Boulesteix J., 2002, *A&A*, 387, 821
- Hancock M., Weistrop D., Eggers D., Nelson C. H., 2003, *AJ*, 125, 1696
- Izotov Y., Stasińska G., Meynet G., Guseva N., Thuan T., 2006, *A&A*, 448, 955
- Katkov I. Y., Chilingarian I. V., 2011, in *Astronomical Society of the Pacific Conference Series*, Vol. 442, *Astronomical Data Analysis Software and Systems XX*, Evans I. N., Accomazzi A., Mink D. J., Rots A. H., eds., p. 143
- Kewley L. J., Groves B., Kauffmann G., Heckman T., 2006, *MNRAS*, 372, 961
- Kroupa P., 2002, *Science*, 295, 82
- Leitherer C. et al., 1999, *ApJS*, 123, 3
- Libeskind N. I., Knebe A., Hoffman Y., Gottlöber S., Yepes G., 2011, *MNRAS*, 418, 336
- Magrini L., Stanghellini L., Corbelli E., Galli D., Villaver E., 2010, *A&A*, 512, A63
- Makarov D., Prugniel P., Terekhova N., Courtois H., Vauglin I., 2014, *A&A*, 570, A13
- Martins L. P., González Delgado R. M., Leitherer C., Cerviño M., Hauschildt P., 2005, *MNRAS*, 358, 49
- Miralles-Caballero D., Díaz A. I., Rosales-Ortega F. F., Pérez-Montero E., Sánchez S. F., 2014, *MNRAS*, 440, 2265
- Moiseev A. V., Tikhonov A. V., Klypin A., 2014, *ArXiv e-prints*:1405.5731
- Pilyugin L., Mattsson L., Vílchez J., Cedrés B., 2009, *MNRAS*, 398, 485
- Pilyugin L., Vílchez J., Thuan T., 2010, *ApJ*, 720, 1738
- Pilyugin L. S., Mattsson L., 2011, *MNRAS*, 412, 1145
- Pilyugin L. S., Thuan T. X., Vílchez J. M., 2007, *MNRAS*, 376, 353
- Renzini A., Andreon S., 2014, *MNRAS*, 444, 3581
- Rupke D. S. N., Kewley L. J., Barnes J. E., 2010, *ApJ*, 710, L156
- Saburova A. S., Zasov A. V., 2012, *Astronomy Letters*, 38, 139
- Sánchez S. F. et al., 2014, *A&A*, 563, A49
- Smith B. J., Giroux M. L., Struck C., Hancock M., 2010, *AJ*, 139, 1212
- Smith B. J. et al., 2008, *AJ*, 135, 2406
- Spitoni E., Calura F., Matteucci F., Recchi S., 2010, *A&A*, 514, A73
- van der Marel R. P., Franx M., 1993, *ApJ*, 407, 525
- van Dokkum P. G., 2001, *PASP*, 113, 1420
- Vázquez G. A., Leitherer C., 2005, *ApJ*, 621, 695
- Werk J. K., Putman M. E., Meurer G. R., Santiago-Figueroa N., 2011, *ApJ*, 735, 71
- Werk J. K., Putman M. E., Meurer G. R., Thilker D. A., Allen R. J., Bland-Hawthorn J., Kravtsov A., Freeman K., 2010, *ApJ*, 715, 656

Zaragoza-Cardiel J. et al., 2013, MNRAS, 432, 998

Zasov A., Kasparova A., 2014, Ap&SS, 353, 595